 doi:10.20944/preprints202008.0675.v1

Article

Storm-induced boulder displacements: inferences from field survey and hydrodynamic equations

Marco Delle Rose [1,*], Corrado Fidelibus [2], Paolo Martano[1] and Luca Orlanducci[3]

[1] Istituto di Scienze dell'Atmosfera e del Clima, Consiglio Nazionale delle Ricerche, Lecce, Italy
[2] Dipartimento di Ingegneria dell'Innovazione, Università del Salento, Lecce, Italy
[3] Geopro, Geological Prospections, Lecce, Italy
* Correspondence: m.dellerose@le.isac.cnr.it

Abstract: The storm of November 12th-13th, 2019 provoked the displacements of boulders in a central Mediterranean rocky coast; with reference to a selected area, prone to the boulder production and geomorphologically monitored for years, a field-oriented study approach was applied for the phenomenon, by collating data concerning pre-storm locations and kinematics of these boulders. The number of displaced boulders is 11, that is, in terms of morphological imprint of a specific storm, one of the major study cases for the Mediterranean. In addition, based on widely used hydrodynamic equations, the minimum wave height required to displace the boulders is assessed. The values conform with the expected values for the wave climate dominating during the causative meteorological event and give a measure of the energy of the storm slamming the coast. Boulder dislodgements usually have plays a key role in determining the rate of the coastal recession, likely also in the investigated area. In view of an adverse climate evolution with a possible increase of energy and frequency of severe storms, the results deriving from the study of this morphodynamics should be considered for the hazard assessment and coastal management.

Keywords: wave impact assessment; characteristic wave height; Salento peninsula; Taranto Gulf; Mediterranean Sea; November 2019 storm.

1. Introduction

For the hazard assessment and defence planning of coastlines reliable data on the impact produced by high-energy waves are required [1,2]. Geological surveys aimed at recognizing such an impact are indispensable in order to acquire data concerning the nearshore [3,4]. Studies of displacement modes and trajectories of boulders based on comparison among pre- and post-event data are of relevance. However, the number of cases documented in the literature is small, being the initial positions of the boulders generally not known (see e.g. [5,6]). Some relevant cases regard the Mediterranean coast [7–9]. The studies of these cases illuminate in view of the prediction of boulder displacements during future storms [10,11].

In the Mediterranean Sea, throughout the second half of the 20th century, moderate storm events prevailed, with peaks of frequency of the cyclones in winter. In the middle of the 70s, the wind activity shifted from a decreasing trend to an increasing one [12,13]. Since the beginning of the new century, the increased occurrence of cyclones with tropical-like characteristics (i.e. medicanes) in the area has raised concerns. On September 26th, 2006, a medicane battered the western coast of the Salento peninsula (southern Italy, central Mediterranean Sea) [14]. A minimum sea level pressure of 986 hPa was registered; it was the lowest in the records of the minimal pressure during similar storms in the whole Mediterranean area [15]. Later, several intense storms hit the Mediterranean causing widespread damages [16–18]. Thus, future modifications of the cyclones are of concern due to the large damage

 doi:10.20944/preprints202008.0675.v1

potential [19,20]. As a consequence of the global warming, it is predicted that at the end of the century the cyclones will last longer and bring stronger winds [21].

In the last few years, the western coast of the Salento peninsula has been affected by more and more severe coastal storms and many infrastructures have been damaged. Large waves have caused dislodgement of rock boulders and breakwater blocks and damage of promenade walls [22]. The October 29, 2018 storm event [17,18] affected also the western coast of Salento peninsula, where caused the displacement of some boulders [23]. One year later, on November 12th-13th, a severe storm (hereinafter called IonicS19) hit again the area with considerable effects. The survey of these effects is the focus of this note. Specifically, the following is reported: (1) a description of the geomorphological imprints on the coast; (2) the inference of the hydrodynamic features of the storm; (3) useful general remarks for the coastal hazard and management issues. The note is structured as a follows: in Section 2, the features of the investigated coastal stretch are reported; in Section 3, IonicS19 is described; in Section 4, the results of the field surveys are shown; in Section 5, an assessment of the waves impact on the coast during the storm event are presented; in Section 6, discussion and conclusion are given. Finally, in Appendix A.1, some specific features of the geomorphological monitoring of the affected area are reported, in Appendix A.2 several details of pre- and post-storm data are explained.

2. Study area

The Salento peninsula belongs to the Apulian Platform, a crustal domain characterized by a horst-and-graben structure, and formed by Cretaceous limestones overlain by Tertiary and Quaternary clastic carbonates and clayey marls. Due to the prevalence of calcareous rocks, the landscape frequently shows karst features. As a whole, the peninsula is a flat plateau gently dipping from south east (mean altitude 100 m a.s.l.) to north west (mean altitude 35 m a.s.l.). Throughout the Middle-Late Pleistocene, the coastal zones were morphed by the interaction between tectonic and eustatic processes [24], resulting in a staircase of marine terraces. The area herein selected for the survey faces the semi-enclosed Taranto Gulf (Figure 1). It has a microtidal regime and is moderately urbanized, crowded in summer for tourism. A breakwater of a small harbor and an abandoned mussel breeding farm constitute the only structures along the coastline. Hundreds of boulders constitute a prominent geomorphological feature of the area; they are isolated or arranged in groups, and scattered on the platform by a catastrophic event, likely a tsunami occurred in 1456 [25].

Preprints (www.preprints.org) | NOT PEER-REVIEWED | Posted: 30 August 2020 doi:10.20944/preprints202008.0675.v1

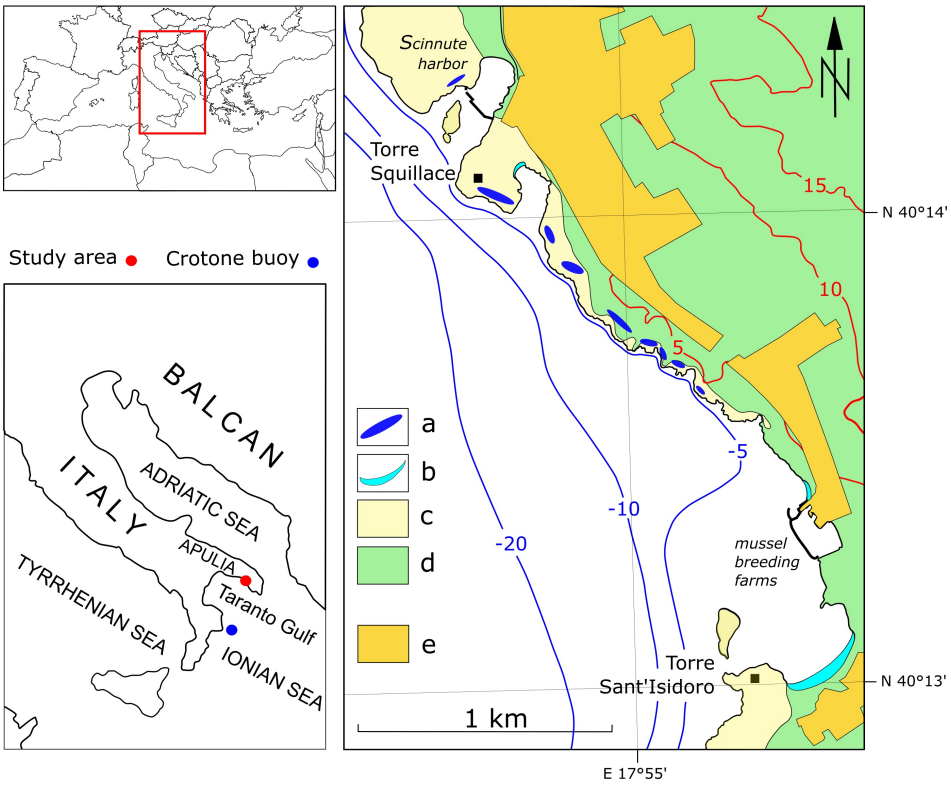

Figure 1. Geological map of the study area (modified from [26]); legend: a, boulder field, b, sandy beach, c, Pleistocene calcarenites, d, Cretaceous limestones; e, urban area; contour lines (red) from the technical map of Lecce Province (1: 5,000), isobaths (blue) from the nautical chart of Istituto Idrografico della Marina Militare (1:100,000).

The coastal area is generally flat, major slopes are close the coastline, especially between -5 m and 5 m a.s.l. The slope of the shoreface, between the isobaths -5 and -20 m, ranges from 1.5 to 6%. The rocky substratum is generally covered by sands settled by benthic communities. Among Torre Squillace and Torre Sant'Isidoro, the cliff is 5 meters high, almost entirely below the sea level, and is interrupted by sandy beaches (Figure 1). A coastal platform, large hundreds of meters, extends inland from the edge of the cliff. On the platform, the paraconcordant contact between Cretaceous limestones and a late Quaternary calcarenitic terrace is visible [27]. These rocks are carved by typical coastal karst forms such as pinnacles and solution pans. More recent continental deposits (lithified eluvium, carbonate breccia) frequently cover the previous formations. Enhanced karst processes, due to brackish groundwater flowing to the sea, cause the formation of collapse dolines and control the morphological evolution of the coastline [28].

Some of the boulders scattered along the surveyed area were maybe moved by storm waves during the last 50-100 years; such a hypothesis is being tested [26]. Moreover, for the peculiar geological features, the site is prone to boulder production, as evident by field observations. Therefore, since 2017, the stretch of the rocky coast between Torre Squillace and Torre Sant'Isidoro (Figure 1) is subjected to geomorphological monitoring with focus on the locations of the boulders (see Appendix A.1). After IonicS19 (see Section 3), the displacements of eleven boulders were defined through a field survey and photographic documentation (see Section 4).

As far as the wave climate is concerned, since 1989 a reference for the Taranto Gulf is the Crotone buoy (Figure 1). It belongs to the Italian ondametric network and is placed offshore (mooring depth 80 m) at the south-western side of the semi-enclosed basin. By analyzing the data of the buoy, the derived value of H_s, the maximum significant wave for a 50-years return period, is 6.3 m [29]. Estimates of H_s for a 100-years return period, resulting from additional processing of the buoy data, are 7.5 and 8.2 m, obtained by using an ECMWF model and a NOAA model, respectively [30].

Preprints (www.preprints.org) | NOT PEER-REVIEWED | Posted: 30 August 2020 doi:10.20944/preprints202008.0675.v1

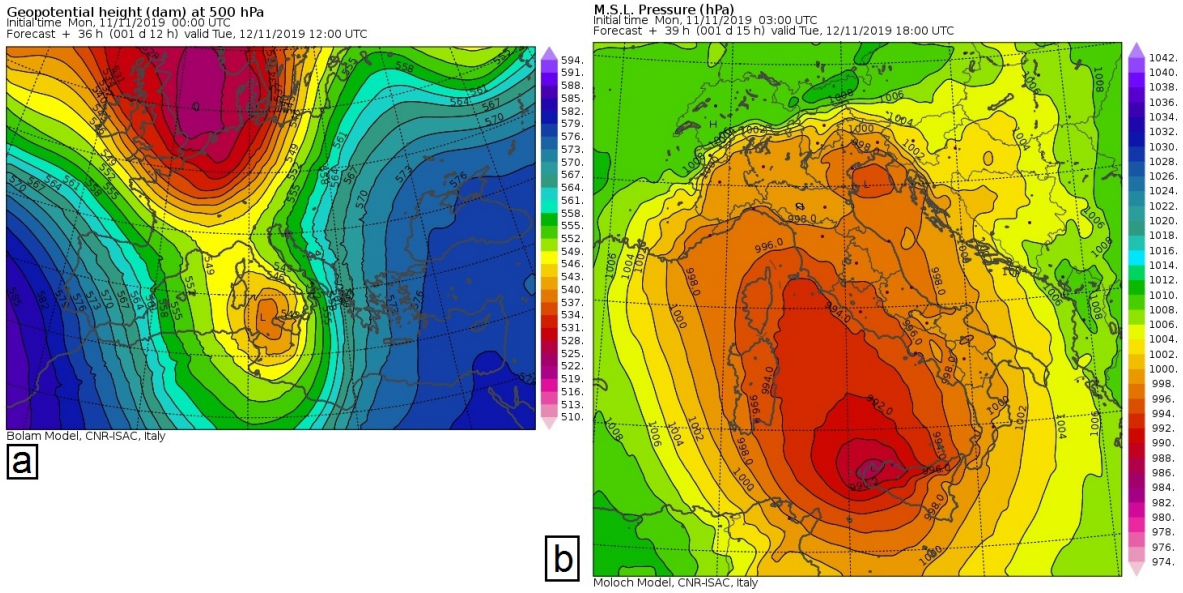

Figure 2. (a) Geopotential height at 500 hPa over the western Mediterranean Sea at 12.00 UTC of November 12, 2019; (b) Surface pressure over the central Mediterranen at 18.00 UTC of November 12, 2019. To be noticed also the secondary minimum over the northern Adriatic; images downloaded from [32].

3. The 11/12-13/2019 storm

For the meteorological overview of the storm, the archive maps of the model cascade GLOBO-BOLAM-MOLOCH of the Institute of Atmospheric Sciences and Climate, National Research Council of Italy (CNR-ISAC) are used [31,32]. Since the first days of the month, a stable configuration of high pressure conditions over the middle Atlantic and the Caspian Sea regions favored the formation of an extended trough at 500 hPa going from the Northern-Central Europe down to the Mediterranean Sea, bringing frequent and quite strong southern winds over the Salento peninsula. On November 5th, a storm with winds blowing at about 12 m/s and at 10 m height offshore impinged over the western Salento coast followed on the 9th by another storm with south-western winds of about 10 m/s. On November 11th, a through at 500 hPa approaching from the north west of France deepened strongly over the Gulf of Lyon, an area that often acts as a feeding area in increasing the strength of the Mediterranean storm in this period of the year. The trough then migrated southward in the Tyrrhenian Sea reaching Sicily after acquiring more strength turning around the Atlas plateau and thus conveying very strong winds over the Taranto Gulf (Figure 2a). IonicS19 was characterized by a deep surface pressure minimum developed over the Tyrrhenian Sea. This caused the development of a secondary minimum on the other side of Italy on the northern Adriatic Sea (Figure2b). This minimum migrated towards the Venice Lagoon and the consequent veering wind among the lagoon boundaries caused a very anomalous surge on different parts of the lagoon, with height often well over 1.5 m, one of the highest of the last decades [33]. In the meantime, some forecast models predicted the evolution of the storm in a medicane [34]. A strong south-eastern wind over the Salento peninsula started soon after midnight from the south east, and persisted for about 12 hours from the same direction with an offshore fetch of about 800 km, down to the Libyan coast (Figure 3). In the following evening, the wind turned S-SW until the afternoon of November 13th, with a fetch reduced to about 350 km, further reducing until the end.

Preprints (www.preprints.org) | NOT PEER-REVIEWED | Posted: 30 August 2020 doi:10.20944/preprints202008.0675.v1

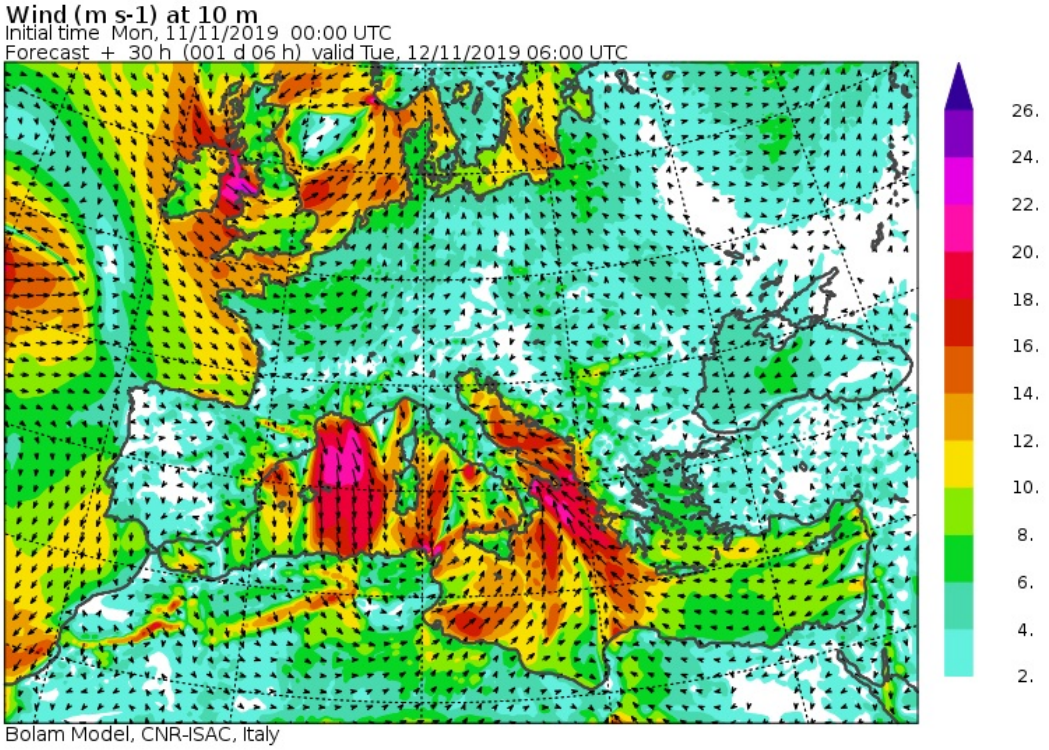

Figure 3. Wind speed at 10 m height on November 12th, 2019 at 6.00 UTC; note the quite long fetch down to the Libyan coast; image downloaded from [32].

IonicS19 caused a number of damages on structures along a 30 kilometers stretch of coast. The most affected places were the city of Gallipoli and the villages of Santa Caterina and Porto Cesareo (Figure 4). Promenade walls were destroyed and breakwater blocks were displaced towards the coastal road. In Gallipoli, several boats sunk and numerous infrastructures along the seafront were destroyed. The largest breakwater block has an estimated volume of 3 m^3 and weighs 8 tons (Figure 4). In addition, as previously mentioned, on the shore platform between Torre Squillace and Torre Sant'Isidoro (Figure 1), eleven boulders were dislodged (see Section 4).

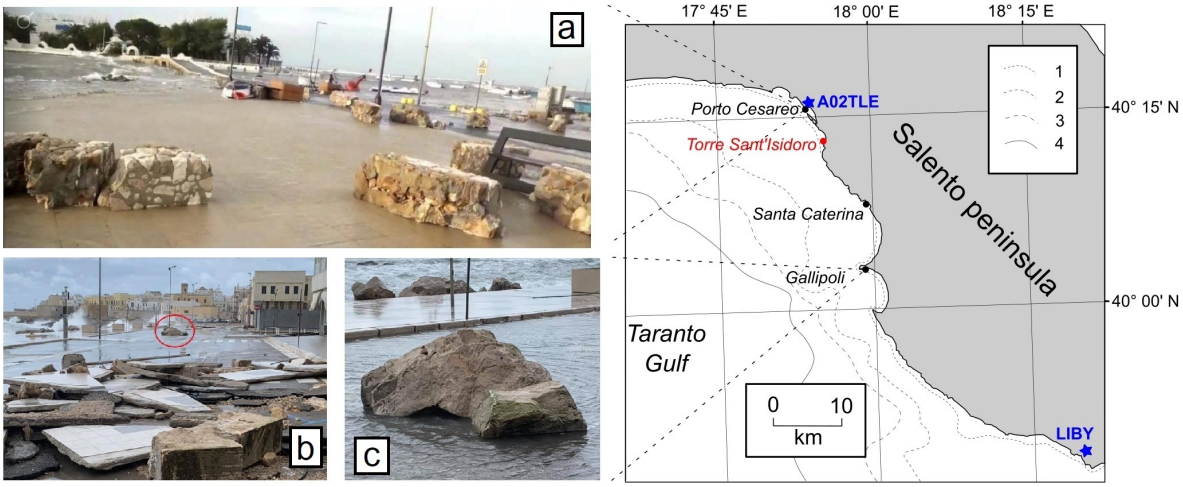

Figure 4. Examples of damages caused by the November 12th-13th, 2019 storm on some urban areas; (a) Porto Cesareo, blocks of a destroyed promenade wall; (b) Gallipoli, blocks of promenade wall and pavement, the red circle marks the largest breakwater block displaced during the storm; (c) close view of the block.

Preprints (www.preprints.org) | NOT PEER-REVIEWED | Posted: 30 August 2020 doi:10.20944/preprints202008.0675.v1

Two data sets are used to describe the wave climate and the wind features. They come from the following stations (Figure 4): the Porto Cesareo wind gauge, a reference station of the Italian Civil Protection Department (local identification codex: A02TLE; elevation 12 m a.s.l.) [35]; the S. Maria di Leuca station, pertaining to the meteorological service of the Italian Air Force and reference station of the World Meteorological Organization (WMO code: 16360; ICAO code: LIBY; elevation 112 m asl) [36]. The wind speed and direction hourly-recorded by the A02TLE wind gauge from November 11th to November 14th are reported in Figure 5. For comparison, the semi-diurnal wind speed and direction hourly-recorded by the LIBY station are reported in Figure 6.

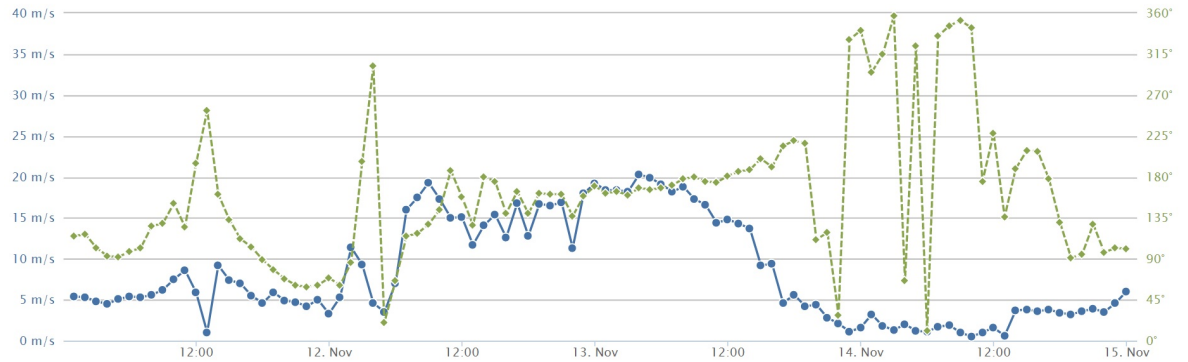

Figure 5. Wind speed and direction (dashed line) hourly-recorded by the A02TLE wind gauge; image downloaded May 16th, 2020, from the SIMOP site of the Apulian Basin Authority (AdBP) [35].

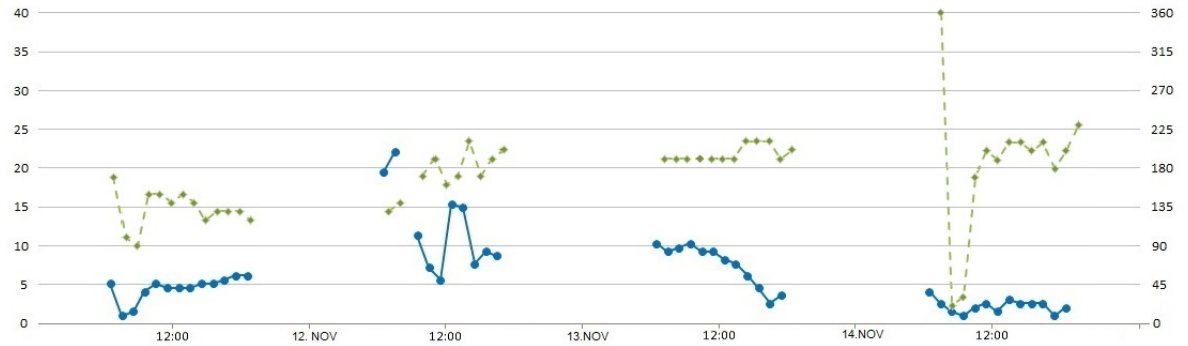

Figure 6. Wind speed and direction (dashed line) hourly-recorded by the LIBY station; image drown using the data downloaded December 11th, 2019, from the OGIMET site [36].

From Figure 5, it is apparent the veering of the wind direction during November 13th. Because of the position of the anemometer, the wind speed is a good proxy for the 10 m height wind speed over the sea, while, with reference to Figure 6, the increased wind speed is due to the height of the LIBY station (112 m a.s.l.).

The following equations have been used to obtain estimates of the wave period T and the characteristic wave height H_{m0}. They relate T and H_{m0} at the wave spectral peak to the wind speed at 10 m height offshore U and to the fetch over the sea F [38] (g is gravity):

$$gT/U = 0.2857(gF/U^2)^{1/3} \quad (1)$$

$$gH_{m0}/U^2 = 0.0016(gF/U^2)^{1/2} \quad (2)$$

The obtained values of T and H_{m0} are 14-15 s and 7-9 m, respectively, with a fetch of 800 km and a wind speed between 15-20 m/s. It must be noted that the characteristic wave height H_{m0} is nearly equivalent to the significant wave height H_s [39,40].

Preprints (www.preprints.org) | NOT PEER-REVIEWED | Posted: 30 August 2020 doi:10.20944/preprints202008.0675.v1

The coastal meteorological stations of the Italian Air Force service, in addition to the wind vectors, also provide semi-diurnal measurements of Sea state (i.e. sea conditions) and Swell wave lengths S_l [41]. These parameters are quantified by means of the aeronautical Q-signals QUK and QUL, respectively, and are correlated with both the Douglas Sea Scale and the Beaufort Wind Force Scale.

The QUK and QUL values, measured by the LIBY station before, during and after IonicS19, are reported in Table 1. From these values, one can infer that the storm intensity grew during the night of November 11th, thus, in the early morning of November 12th, a peak of 9 for QUK was measured, corresponding to an estimate of more than 14 m for H_s. In the meantime, the swell length exceeded 200 m (very high S_l description). The storm, as recorded by the LIBY station, gradually lost strength on November 13th. The large estimates of H_s (>14 m and 9-14 m) in Table 1 seem overestimated, compared to the value of H_{m0} (7-9 m) calculated by means of Eq. 2. However, the QUK data come from "experienced observers" estimation of the 30% highest waves during direct observation of the sea surface.

Table 1. QUK and QUL signals hourly-recorded by the LIBY station in November 2019; data downloaded December 11th, 2019 from the OGIMET site [36], (UTC time).

day/hours	QUK	H_s[m]	QUL	S_l description
11/14.00-16.00	3	0.5-1.25	2	low
11-12/17.00-05.00	no data	-	no data	-
12/06.00-13.00	9	>14	8	very high
12/15.00-16.00	8	9-14	7	high
12-13/17.00-05.00	no data	-	no data	-
13/06.00-12.00	8	9-14	7	high
13/13.00-14.00	7	6-9	6	rough
13/15.00-16.00	5	2.5-4	3	light
13-14/17.00-05.00	no data	-	no data	-
14/06.00-07.00	2	0.1-0.5	1	very low

4. Data of the field surveys

The displacements of the eleven boulders caused by IonicS19 were identified by means of: (1) a recognition of the detached surfaces (the so-called "sockets" [42]); (2) a comparison of transect photos taken before and after the storm, respectively; (3) marks of the displacements on the joints previously bounding the boulders. The locations of the investigated boulders are shown in Figure 7. They are all placed in the central sector of the investigated area, inside the splash-spray zone; the relative locations are reported in Table 2, together with pre-storm locations.

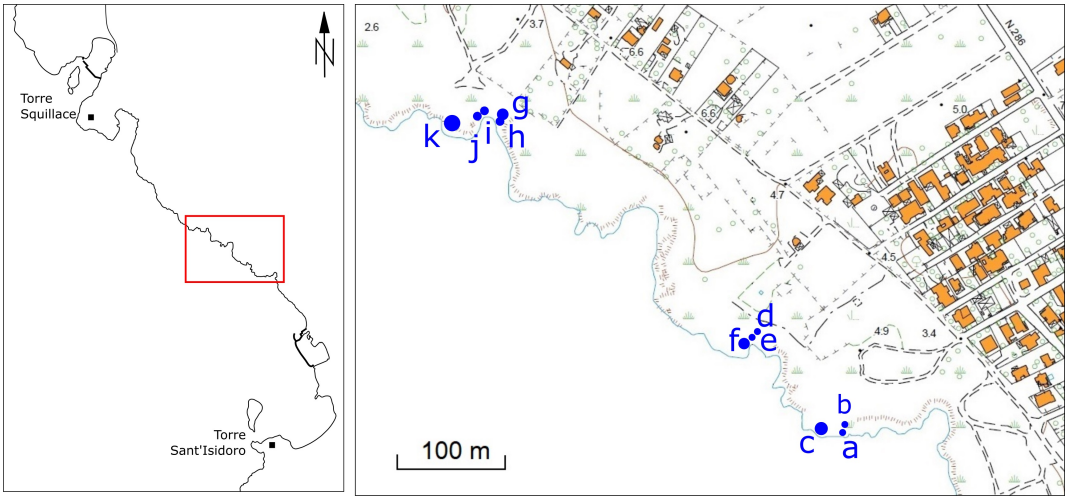

Figure 7. Locations of the boulders displaced by the November 12-13, 2019 storm. Topography from technical map of the Lecce Province (1: 5,000).

Preprints (www.preprints.org) | NOT PEER-REVIEWED | Posted: 30 August 2020 doi:10.20944/preprints202008.0675.v1

Table 2. Pre- and post- geographical coordinates of the displaced boulders; ind., indeterminable.

boulder ID	pre-storm location latitude	longitude	post-storm location latitude	longitude
SI19a	40°13′34.09"N	17°55′17.79"E	ind.	ind.
SI19b	40°13′34.25"N	17°55′17.83"E	40°13′34.22"N	17°55′17.82"E
SI19c	40°13′34.20"N	17°55′17.51"E	ind.	ind.
SI19d	40°13′37.03"N	17°55′14.06"E	40°13′37.20"N	17°55′14.28"E
SI19e	40°13′36.97"N	17°55′14.01"E	40°13′37.05"N	17°55′14.16"E
SI19f	40°13′37.03"N	17°55′14.06"E	40°13′37.04"N	17°55′14.07"E
SI19g	40°13′43.82"N	17°55′05.10"E	40°13′43.89"N	17°55′05.12"E
SI19h	40°13′43.81"N	17°55′05.09"E	ind.	ind.
SI19i	40°13′44.07"N	17°55′04.60"E	ind.	ind.
SI19j	40°13′44.05"N	17°55′04.59"E	40°13′44.21"N	17°55′04.72"E
SI19k	40°13′43.81"N	17°55′02.97"E	40°13′43.81"N	17°55′02.97"E

The post-storm locations of SI19a, SI19c, SI19h, and SI19i were not recognized. The lengths a, b and c of the axes of each boulder (assumed prismatic) are reported in Table 3, together with the distances x and x_f from the cliff edge, respectively pre-storm and post-storm. Boulder dimensions are determined according to rules defined in the literature [37].

Table 3. Dimensions of the boulder axes a,b,c, pre-storm distances from the cliff x, post-storm distances from the cliff x_f, BT, Boulder Type: JB, Joint-Bounded, SA, Sub-Aerial (not joint-bounded); MT, Movement Type: ST, saltation, SL, sliding, OV, overturning; ind., indeterminable.

	a[m]	b[m]	c[m]	x[m]	x_f[m]	BT	MT
SI19a	0.6	0.6	0.4	0.5	ind.	SA	ind.
SI19b	1.6	1.2	0.3	8.5	6.5	SA	ST
SI19c	2.6	1.7	0.6	1.5	ind.	SA	SL
SI19d	1.3	1.1	0.4	12	19.5	SA	ST
SI19e	2.3	0.7	0.6	11	16.5	JB	ST
SI19f	2.8	2.4	0.4	12	12.5	SA	ST
SI19g	1.7	1.5	0.5	9	11.5	SA	OV
SI19h	1.1	0.7	0.4	8	ind.	JB	ST
SI19i	1	0.8	0.7	17	ind.	SA	ind.
SI19j	1,2	0,8	0,6	18,5	22	SA	ind.
SI19k	4.8	2.2	1.1	8.0	8.2	JB	ST

In what follows, several evidences of the boulder displacements are presented. Supplementary field data are in Appendix A.2. Boulders SI19a, SI19b, SI19c[1] are at the south-east side of the investigated coastal stretch (Figure 7). Boulders a, b and c (from here 'a', 'b', etc. instead of SI19a, SI19b, etc.) were identified through inspection of the sockets; for boulders a and c, photo-comparisons confirmed the field evidences (Figure A2). Furthermore, for c, drag marks due to the sliding on the platform were identified. The trajectory ends into the sea (Figure A3). In Figure 8 the comparison between the c locations pre- and post-storm are shown.

[1] SI19c coincides with boulder B1 of [26].

Preprints (www.preprints.org) | NOT PEER-REVIEWED | Posted: 30 August 2020 doi:10.20944/preprints202008.0675.v1

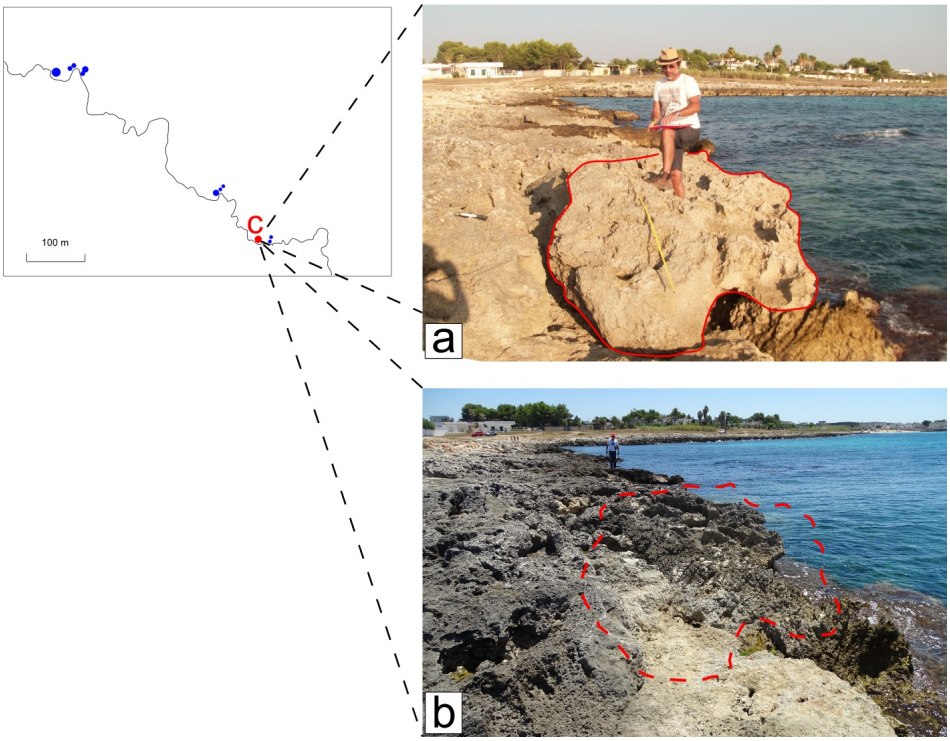

Figure 8. Pre- and post- storm event states; (a) photo taken before the storm, boulder c is marked by the continuous line; (b) photo taken after the storm, the pre-storm position is marked by the dashed line.

The storm-induced displacements of boulders d, e, and f (Figure 7) can be easily detected by considering the field evidences. Note that boulders d and f result from the break of one pre-existing boulder[2] (for details see Figure A4). The boulder displacements can be defined also through the comparison of transect photos (Figure A5). Due to IonicS19, boulder f underwent a short saltation (0.5 m), while boulder d was displaced of 7.5 m (Table 3). Boulder e jumped f, as indicated by the detachment niche (i.e. socket), the marks over the f surface and the e final position (Figure 9).

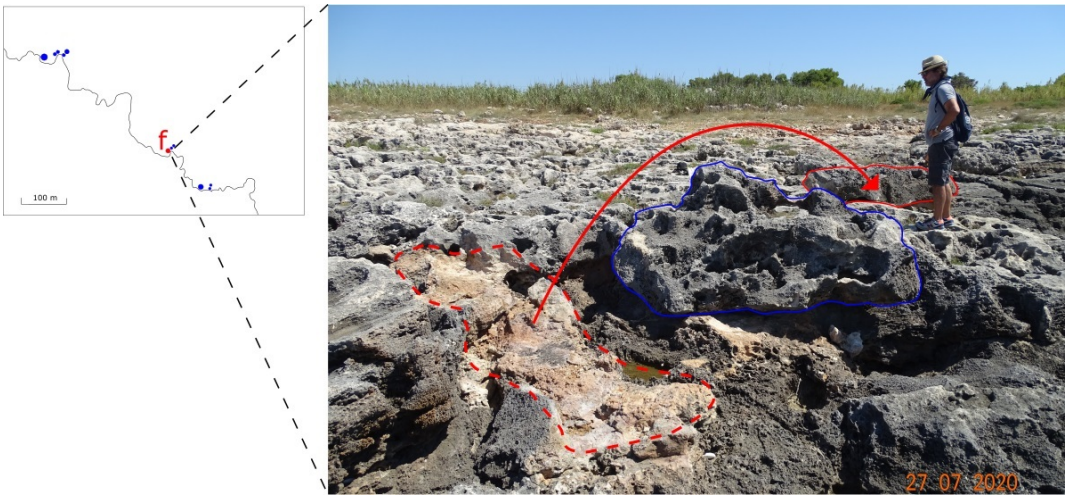

Figure 9. The saltation movement of boulder e; the socket (red dashed) and the final position (red solid) are shown; the blue line highlights boulder f.

[2] Pre-existing boulder is named B2 in [26].

Preprints (www.preprints.org) | NOT PEER-REVIEWED | Posted: 30 August 2020 doi:10.20944/preprints202008.0675.v1

The displacements of g, h, i, j, and k (Figure 7) were kinematically different. By comparison of transect photos (Figure A6) and by field observations, it is apparent that g overturned. Boulders h and i disappeared after the storm. Boulder j was displaced of 3.5 m. Finally, boulder k (Figure 10), the largest of the eleven boulders, underwent a short saltation (Table 3). Failures on the rock surfaces for the high disruptive stresses caused several rock wedges to be detached from the bedrock and the boulder. This feature was decisive for the recognition of k (Figure A7).

Figure 10. Photo of boulder k taken parallel to the $b \times c$ plane; the arrows indicate the shear failures on the rocky surfaces.

5. Hydrodynamics equations

To alternatively quantify the impact of the storm, hydrodynamic equations are applied to estimate the minimum energy of a solitary wave necessary for a boulder displacement. The energy is expressed in terms of (minimum) height H_m. According to [43], for joint-bounded and sub-aerial (non joint-bounded) boulders transported by saltation, H_m is, respectively:

$$H_m \geq \frac{2c\,(\gamma_r/\gamma_w - 1)\,(\cos\theta + \mu_s \sin\theta)}{C_L} \tag{3}$$

$$H_m \geq \frac{2c\,(\gamma_r/\gamma_w - 1)\cos\theta}{C_L} \tag{4}$$

where γ_r and γ_w are the unit weights of rock and water, respectively, μ_s is the coefficient of static friction along rock surfaces, θ is the bed slope angle and C_L is the lift coefficient. For sub-aerial boulders transported by sliding and by overturning, [43] proposed, respectively:

$$H_m \geq \frac{2c\,(\gamma_r/\gamma_w - 1)\,(\mu_d \cos\theta + \sin\theta)}{C_D(c/b) + (\mu_s C_L)} \tag{5}$$

$$H_m \geq \frac{2c\,(\gamma_r/\gamma_w - 1)\,(\cos\theta + (c/b)\sin\theta)}{C_D\,(c^2/b^2) + C_L} \tag{6}$$

where μ_d is the coefficient of dynamic friction [44] and C_D is the drag coefficient.

Alternatively, according to [45], H_m for joint-bounded boulders and sub-aerial boulders is, respectively:

$$H_m \geq \frac{2V\,(\gamma_r - \gamma_w)\,(\cos\theta + \mu_s \sin\theta)}{C_L(acq)\gamma_w} \tag{7}$$

$$H_m \geq \frac{2\mu V \gamma_r}{C_D(acq)\gamma_w} \tag{8}$$

where V is the boulder volume and q is the boulder area coefficient.

Preprints (www.preprints.org) | NOT PEER-REVIEWED | Posted: 30 August 2020 doi:10.20944/preprints202008.0675.v1

Literature data are used herein for a proper choice of the values of the coefficients in Eqs. 5-8; the selected values are: μ_s=0.65, μ_d=0.6, C_L=0.178, C_D=1.95, q=0.73 [4,8,43–46]. The bed slope angle θ is assumed zero due to the very flat morphology of the study area, thus Eq. 3 coincides with the equation (5) proposed by [47], adapted for storm wave. The results are shown in Table 4.

Table 4. Minimum wave heights H_m required to displace the boulders.

	Nandasena et al. (2011)	Engel and May (2012)
SI19a	3.59	0.98
SI19b	2.70	1.97
SI19c	0.72	2.79
SI19d	3.59	1.80
SI19e	5.39	8.62
SI19f	3.59	3.94
SI19g	1.20	2.46
SI19h	3.59	8.62
SI19i	6.29	1.31
SI19j	5.39	1.31
SI19k	9.90	27.10

6. Discussion and Conclusion

On November 12th, 2019, IonicS19 hit battered the western coast of the Salento peninsula moving from SE to NW (Section 3). It severely struck the city of Gallipoli, where the most significant signature was the displacement of a breakwater block having an estimated volume of 3 m^3 and a weight of 8 tons (Figure 4). As recorded by the A02TLE wind station, the storm reached the study area in the early morning (Figure 5). At Porto Cesareo, the wind speed did not exceeded 21 m/s. However, wind persisted for about 12 hours from SE with an offshore fetch of about 800 km (Figure 3). Between Torre Sant'Isidoro and Torre Squillace (Figure 1), the storm caused the displacement of eleven boulders (Section 4). Their size range from 0.6×0.6×0.4 m^3 to 4.8×2.2×1.1 m^3 (Table 3). For six out of eight boulders, the kinematics is saltation (for three boulders the type of movements was not determined). The displacements were roughly normal to the coastline, except for one boulder that travelled an alongshore trajectory as shown by drag marks (Figure A3).

Probably, boulders c and f were already moved by previous storms of the last 50-100 years [26]. If this hypothesis were confirmed, the proneness to the boulder production of the investigated stretch of coast, as inferred from field evidences, would be further proven. Especially in the central sector of the coast between Torre Squillace and Torre Sant'Isidoro, where the base of the Quaternary calcarenite crops out, the boulder production seems to be eased (Figure 7). However, the variability alongshore of the wave energy transfer should be considered. In fact, the effects of the local bathymetry may be larger than the effects of the regional-scale coastal morphology, which are in general assumed dominant. For example, [48] found significant variations in wave energy transmission over short distances (about 100 m) due to the foreshore features, thus suggesting a similar scale of variation for the coastal recession rate.

As previously mentioned (Section 5), the minimum wave height H_m required to displace the boulders (Table 4) may give a measure of the wave energy impact on the coast, as proposed by several authors [4,8,46]. With reference to Table 4, it is to note that the two sets of equations furnish different results. With the exception of boulder k, H_m results always lower than 9 m, corresponding to the maximum characteristic wave height H_{m0} as estimated by Eq. 2. By using Eqs. 3, 4, 5 and 6, H_m values even close to 6 m are obtained, while, by using Eqs. 7 and 8 H_m does not exceed 4 m, except for boulders e, h, and k. However, it is to remark that these hydrodynamic equations have limitations. [49] point out that, apart from flaws in the formulas, the estimation of both C_L and C_D is critical, therefore, instead than applying values excerpted from the literature the estimation should be accomplished with strict reference to the local physical conditions.

 doi:10.20944/preprints202008.0675.v1

Other results in Table 4 deserve comments. An impacting wave only 1.2m high is required to overturn boulder g (Eq. 6), thus, even a slightly rough sea condition was predisposing the boulder to overturn. Actually, a boulder must overcome the roughness in its vicinity to reach a position suitable to the overturning [50]. By a detailed observation of the micro-topography along the transect normal to the coast and crossing the position of boulder g, the effect of this process on the boulder displacement may be advanced. There is a critical angle (Figure A8) that has to be exceeded for the overturning.

As far as boulder k (the largest one) is concerned, a displacement of 0.2 m has been measured during the field survey (Figures 10, A7). As comparison term, for the other boulders, the displacement range between 0.5 m and 7.5 m (computed as difference between final and initial position; see Table 3). By using Eq. 7, the wave height required to displace boulder k seems overestimated. Similar considerations are reported in the literature [8,46]. Instead, Eq. 3 furnishes a more plausible value and suggests that deep-water waves can hit the coast with small changes in wave height. By applying the formulas to the breakwater block displaced at Gallipoli (Figure 4), the resulting H_m values are: 12.13 m with both Eq. 3 and Eq. 4, 2.13 m with Eq. 7 and 16 m with Eq. 8. Again, the equations of [43] return more plausible results, suggesting a greater impact on Gallipoli coast than on the investigated area, as confirmed by the values of QUK recorded at the LIBY station (Table 1).

Anyway, caution is recommended in descending conclusions from Table 4. The equations for boulder displacements provoked by solitary waves were reexamined by [57]. The authors emphasized the strong influence of non-dimensional factors on the results, especially of the ratio between the axes of the boulder in the wave plane. On the other hand, camera monitoring of the effects produced by storms on rocky coasts suggest that the occurrence of boulder displacement is the result of the "impact of multiple small waves rather than of a singular big one" [9]. In respect to the possible actions of multiple waves, an increase of a wave height up to a factor of 5 may be also considered [58].

A process that supposedly contributed to the displacement of k is the hydraulic fracturing as described by [51]. The wave impact on a cliff may induce intense fluid pressures in the rock discontinuities as they are filled with water during wave runup and overtopping (Figure A7b). The pressurisation is repeated and may lead to failures for fatigue with consequent detachment of rock slabs, free to displace. Another process potentially involved could be the development of an overtopping bore [52–54], occurring when large waves overtop sloping beaches, coastal cliffs or defense structures and move inland like bore flows. The studies of this phenomenon in relation to the production and movement of coastal boulders are increasing [55,56]. In other contributions of the authors, the process is analyzed and quantified by resorting to specific hydrodynamic equations.

As far as the morphodynamic evolution of the studied coast is concerned, by considering that the current sea level was reached in six thousand years after the end of the last eustatic rise, the boulder displacements may have strongly contributed to the recession rate. Such displacements are nonlinear and depend on physical, chemical and biological phenomena acting at different temporal and spatial scales. However, storms may give rise to high boulder productions in thousands of years, especially where soft rocks crop out as in the case herein exposed [59,60].

In view of an adverse climate evolution with a corresponding increase of storm intensities and frequency, the investigated morphodynamics process must be carefully evaluated for proper hazard assessment and coastal management. The increasing risks due to the storm events seem confirmed by the last decade records of the LIBY station (Section 3; Figure 4 for location). In fact, the number of stormy days is increased in the past four years; in the same period, the energy of extreme events is also increased (Figure 11).

Preprints (www.preprints.org) | NOT PEER-REVIEWED | Posted: 30 August 2020 doi:10.20944/preprints202008.0675.v1

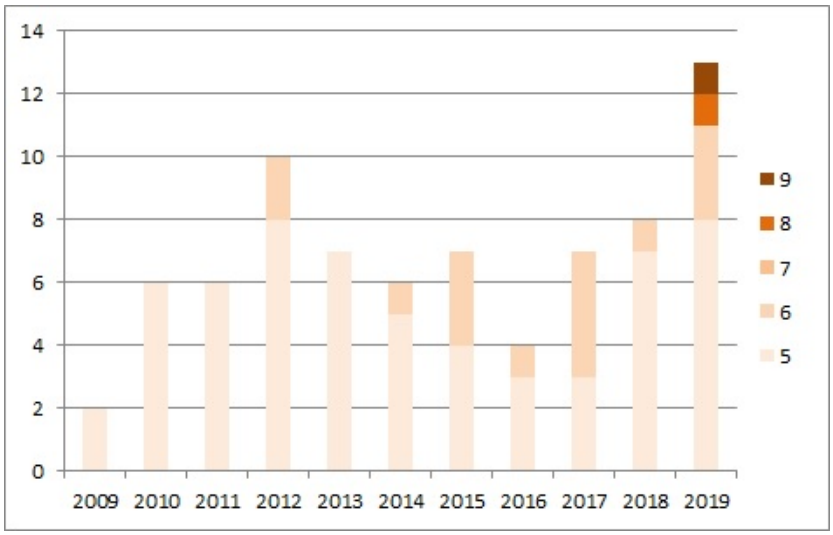

Figure 11. Stormy days occurred in the 2009-2019 as recorded at the LIBY station. The considered thresholds are a duration of more than 6 hours and QUK≥5. Image elaborated by data downloaded by OGIMET site [36].

The stretch of coast under investigation is characterized by a high production of boulders, so the need of a continuous monitoring emerges. Repeated field surveys were functional in order to verify the mobility of the boulders as a consequence of the storms. In the next few years, geomorphological monitoring will continue and will be finally supported by a GIS system.

Author Contributions: Conceptualization, methodology: MDR, CF, PM, LO; field investigation: MDR and LO; meteorological data curating: PM; writing drafts: MDR; writing, review and editing: MDR, CF, PM. All authors have read and agreed to the published version of the manuscript.

Funding: This research received no external funding.

Acknowledgments: The authors wish to acknowledge L. Ciricugno (ISAC-CNR) for the assistance in the photographic survey.

Conflicts of Interest: The authors declare no conflict of interest.

Appendix A.

Appendix A.1. Geomorphological monitoring area

The geomorphological surveys of the Sant'Isidoro-Torre Squillace area begun in 2017. Position, dimensions, orientations (strike and dip) of the $a \times b$ planes, distance from the cliff edge and micro-morphological features of all the boulders larger than 0.5 m^3 were acquired during multiple surveys. The collected data are included in a database to be linked to a GIS. Field surveys were accomplished after each storm since September 2018. The geomorphological effects of the storm of November 12th-13th, 2019, were right away verified. Due to the bad weather conditions and the lock-down following CoViD-19 pandemic, the post-storm survey ended in July 2020.

In Figure A1 the boulder fields of the area are mapped. They were studied with focus on the geomorphological setting. For example, in Figure A1, a group of imbricated boulders positioned along the edge of a collapse sinkhole are shown. One of the objectives of the ongoing research is to establish the chronology of the geomorphological events that led to this arrangement.

 doi:10.20944/preprints202008.0675.v1

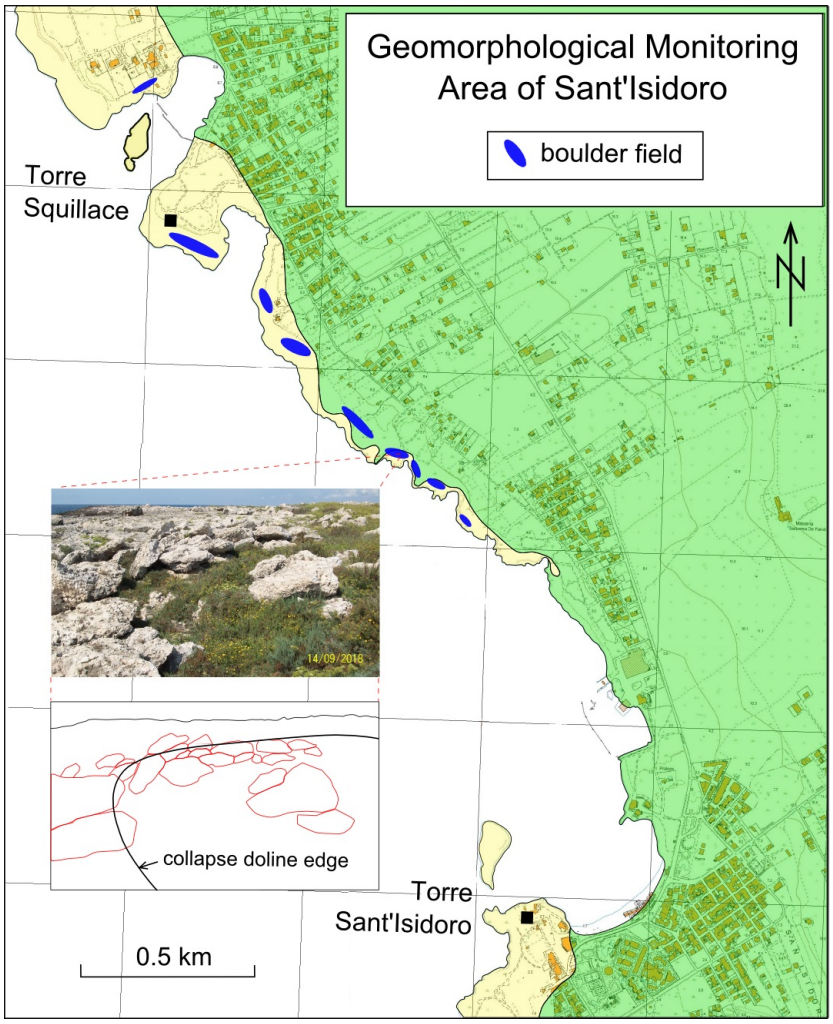

Figure A1. Geological map of the monitoring area with the location of the boulders fields (see Figure 1 for legend); a group of imbricated boulders on a doline edge is clearly visible in the pictures.

A further development of the research will be the study of the sedimentological effects of the storms on pebbles and small boulders inside the bay, by means of structure-from-motion photogrammetry techniques.

Appendix A.2. Boulder displacements features

Field survey details and data supplemental to the Section 4 are reported in what follows. In Figure A2 the comparison between the pre- and post-storm states of a short stretch of coast is shown. It is remark the lack of boulders a and c.

Preprints (www.preprints.org) | NOT PEER-REVIEWED | Posted: 30 August 2020 doi:10.20944/preprints202008.0675.v1

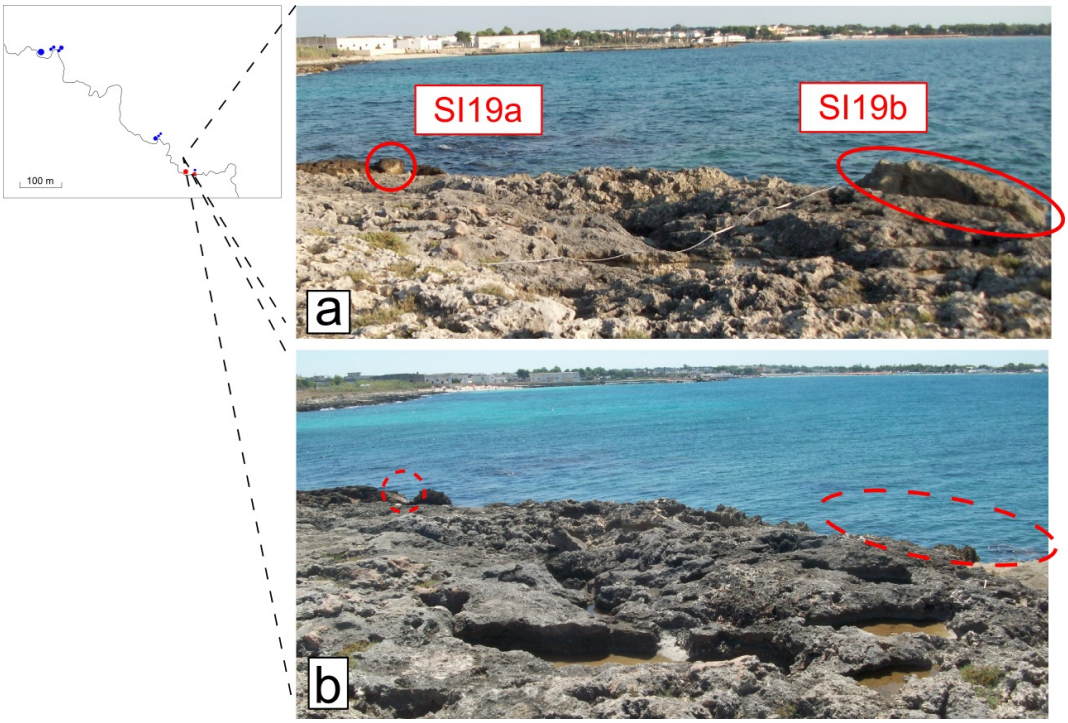

Figure A2. Comparison between pre- and post- storm event states; (a) photo taken before the storm with boulders a and c; (b) photo taken after the storm; the lack of the boulders is highlighted by the dashed lines.

In Figure A3 evidences of the displacements of boulders b and c are shown. Note that boulder c is visible on a pre- storm satellite image of Google Earth (Figure A3a). The sliding of c due to the waves impact during IonicS19 is pointed out by drag marks over the platform (Figure A3b). These marks cross the coastline, thus the inferred trajectory of c ends into the sea (Figure A3c). Despite its small size and the proximity to the cliff edge (Table 3), boulder b was displaced of 2 m only (Figure A3d).

Preprints (www.preprints.org) | NOT PEER-REVIEWED | Posted: 30 August 2020 doi:10.20944/preprints202008.0675.v1

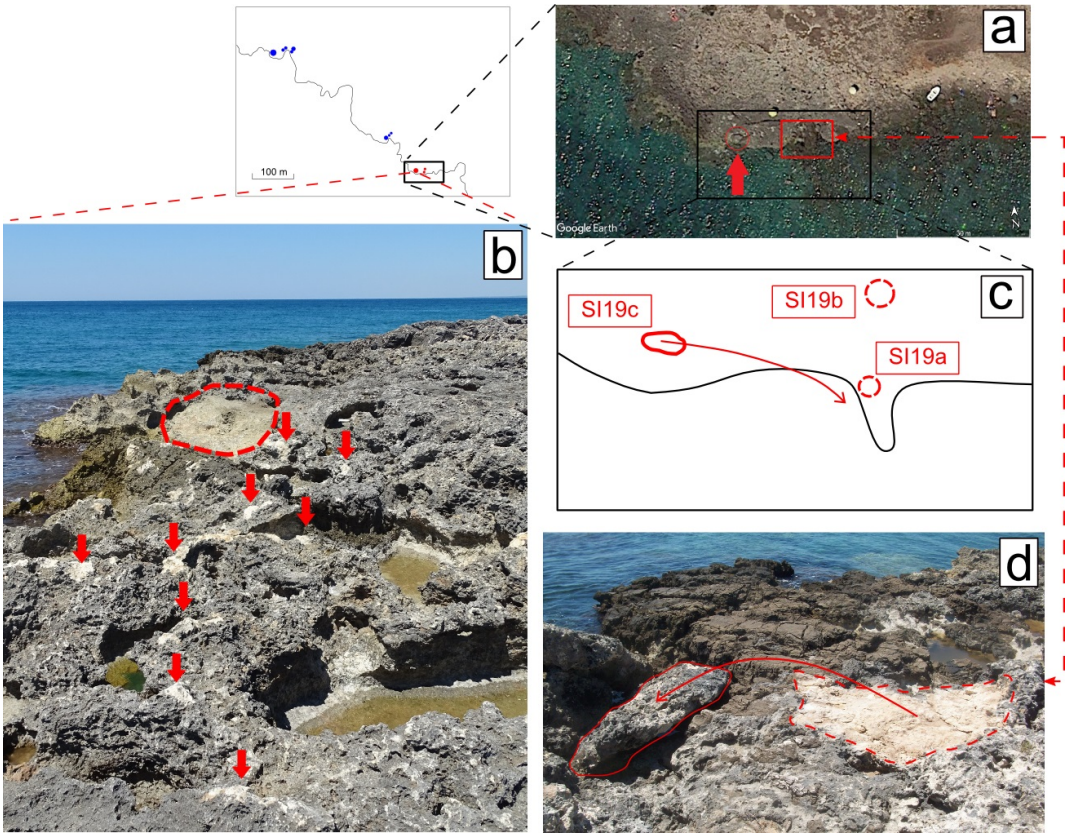

Figure A3. Evidences of geomorphological imprints on the surveyed area of the storm of November 12th-13th, 2019; (a) 2015 Google Earth satellite image with the location of boulder c; (b) drag marks for the sliding of boulder c (the dashed line marks the pre-storm location); (c) the inferred trajectory of c as defined through the field survey; (d) the socket and the post-storm location of boulder b (the supposed saltation movement is also drawn).

As above reported (Section 4), boulders d and f result from the the break of one pre-existing boulder (named B2 by [26]), due to IonicS19. Boulder d has a volume of just over 0.5 m^3, while boulder f has a volume of 2.7 m^3 (Table 3). The latter has been displaced for 0.5 m (thus, it currently has almost the same position of B2) and is visible on the satellite images of Google Earth (Figure A4a). The fracture along which the two boulders separated is highlighted in Figure A4b, while in Figure A4c a perspective view of the boulders d, e, and f can be observed.

Preprints (www.preprints.org) | NOT PEER-REVIEWED | Posted: 30 August 2020 doi:10.20944/preprints202008.0675.v1

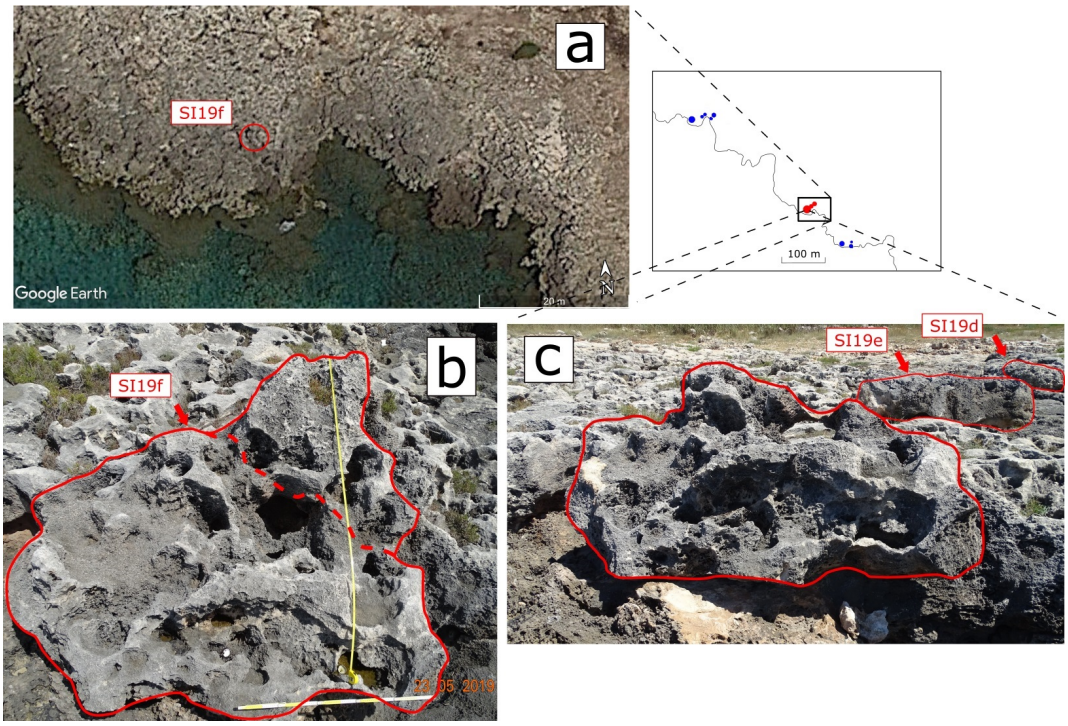

Figure A4. Comparison between pre- and post- storm event states; (a) 2015 Google Earth satellite image with the location of boulder f; (b) pre-storm image of the boulder with the new fracture; (c) post-storm image of f (note the change of shape) with boulders d and e on the background. The fresh unweathered rock surface under the boulder is part of the socket.

In Figure A5, a comparison between the pre- and post-storm states of the zone of boulders d, e, and f is reported. The transect photo of Figure A5a documents the post- IonicS19 state of the site. One can observe the current positions of the boulders, and the sockets of the boulders e and f. The pre-IonicS19 is documented by Figure A5b,c. In the latter, the fracture causing the break of the boulder B2 of [26] is highlighted.

Preprints (www.preprints.org) | NOT PEER-REVIEWED | Posted: 30 August 2020 doi:10.20944/preprints202008.0675.v1

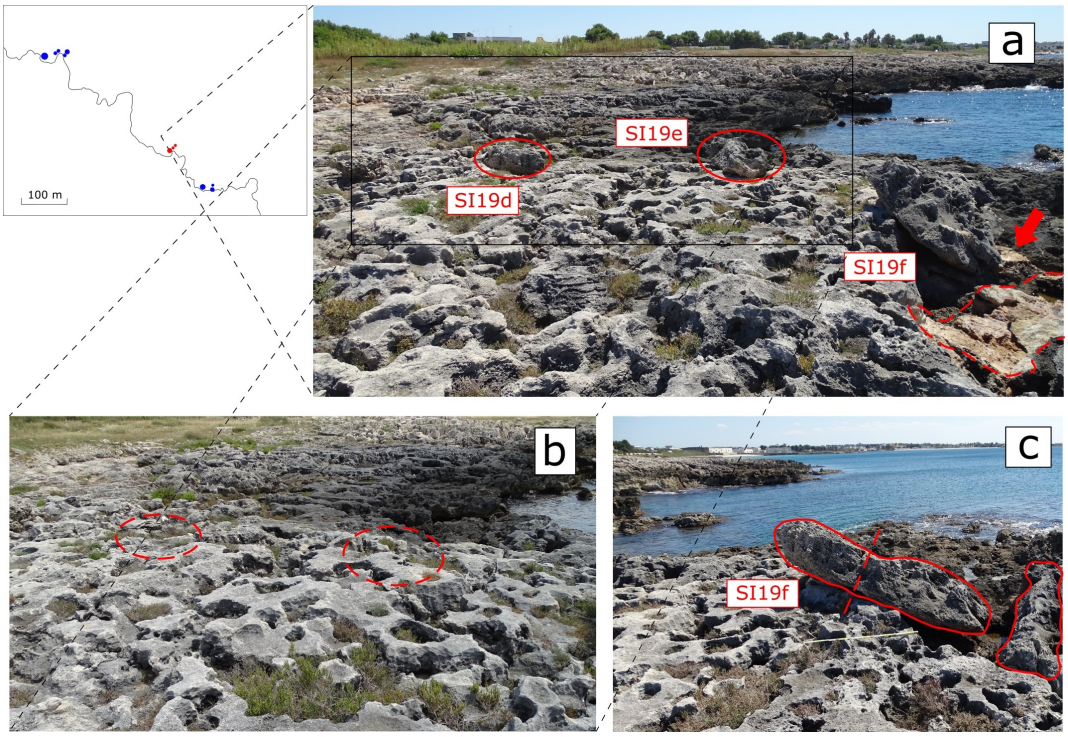

Figure A5. Comparison between pre- and post- storm states; (a) post-storm state of the zone of boulders d, e, and f, the socket of boulder f (red arrow), the socket of boulder e (dashed line); (b) pre-storm state (the post-storm locations of boulders d and e are marked by dashed lines); (c) a pre-storm image of boulder f with the fracture caused by the storm, the initial location (solid line) of boulder e.

306 Also boulders g and k are visible on the satellite images of Google Earth (Figure A6a). The
307 transects of Figures A6b,c allow an easy comparison among pre- and post- storm event.

Preprints (www.preprints.org) | NOT PEER-REVIEWED | Posted: 30 August 2020 doi:10.20944/preprints202008.0675.v1

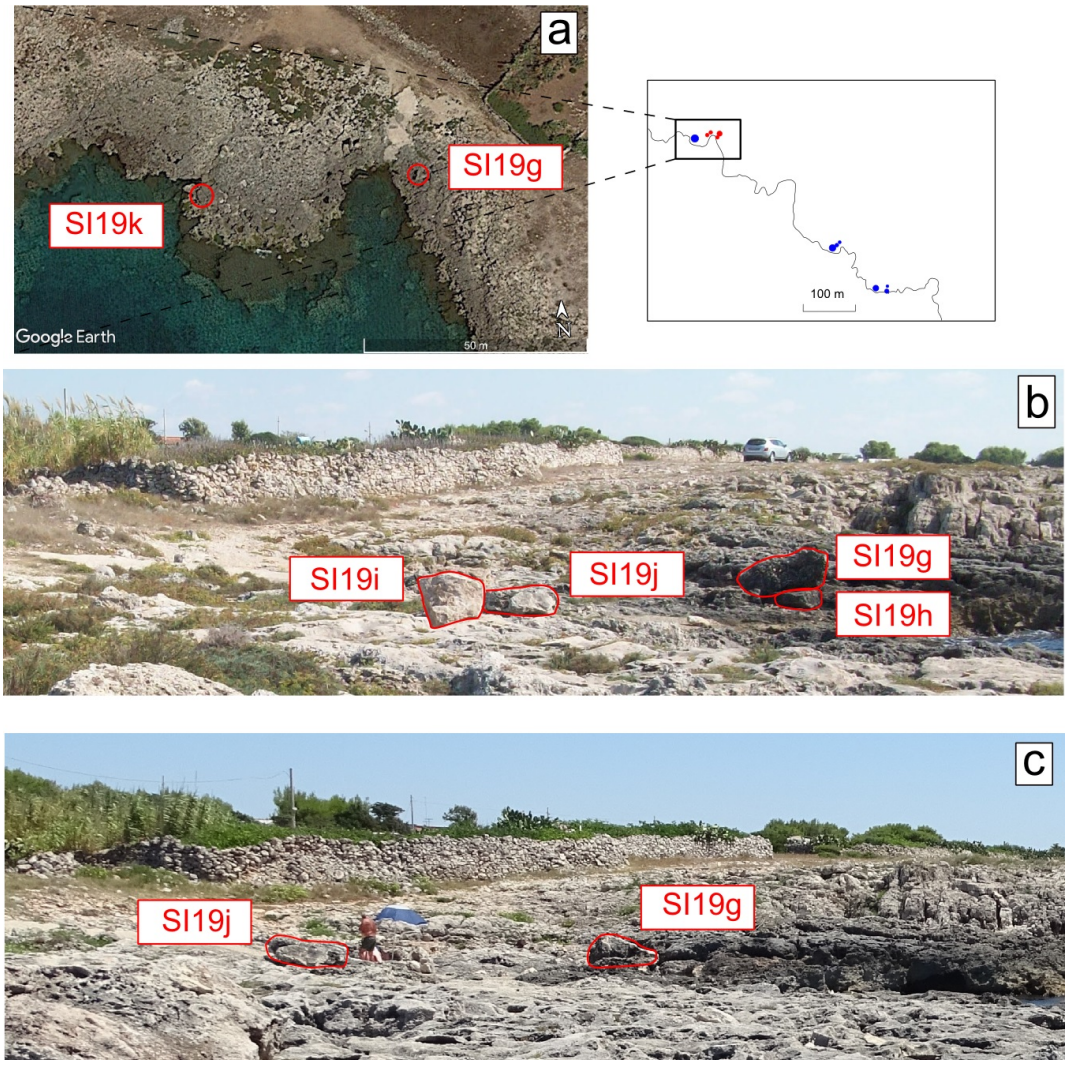

Figure A6. Comparison between pre- and post- storm event states; (a) 2015 Google Earth satellite image with the locations of boulders; (b) pre-storm location of boulders g, h, i, and j; (c) post-storm locations, note that boulders h and i are missing.

By observing the rock wedges detached from the bedrock, the imprint of the storm on boulder k was detected (Section 4). The boulder was first detached from the rock mass. A fracture propagation can be advanced as cause of the detachment. In Figure A7 an explicative sketch is shown. Presumably, two non persistent rock mass fractures (dashed lines in the sketch) were propped open by the high water pressures generated by the wave. Regarding the geological nature of the fractures, the horizontal one is a stratification plane while the sub-vertical one is of tectonic origin. The rock bridges of these fractures were disrupted (a tensile failure occurred) and the block was separated by the rock mass. The high pressures from the top of the sub-vertical fracture laterally pushed the wedges that slid once the shear strength on the fractures was reached. It is worth to mention that, in case the fractures are not submerged, the water of the wave pressurises the air inside the fractures with a sort of piston effect, with an increased damaging impact [61].

Preprints (www.preprints.org) | NOT PEER-REVIEWED | Posted: 30 August 2020 doi:10.20944/preprints202008.0675.v1

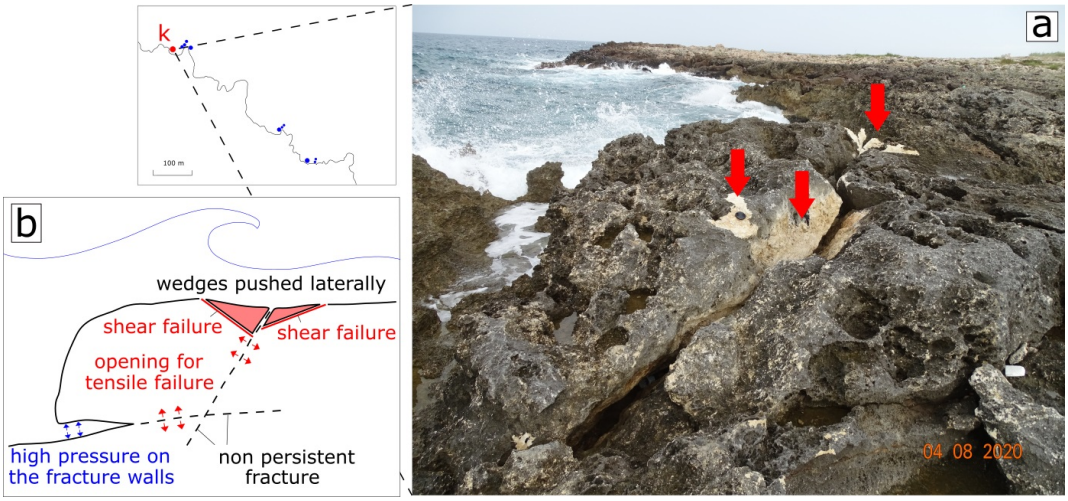

Figure A7. Details of the detachment surfaces of the rock wedges dislodged by boulder k during the November 12-13, 2019 storm. (a) the detached surfaces indicated by arrows; (b) sketch of the fracturing process with the new fractures and the detached rock wedges.

Boulders g and h, in Sub-Aerial and in Joint-Bounded conditions, respectively (Table 3), had different fates (Section 4). Initially, one overlapped the other (Figure A8), then g was found overturned, while h was not found after the storm. There are no clues to understand if the movements took place at the same time. However, the overturning of g was possible after the exceeding of the critical angle θ_c (Section 6, Figure A8) as shown by [50].

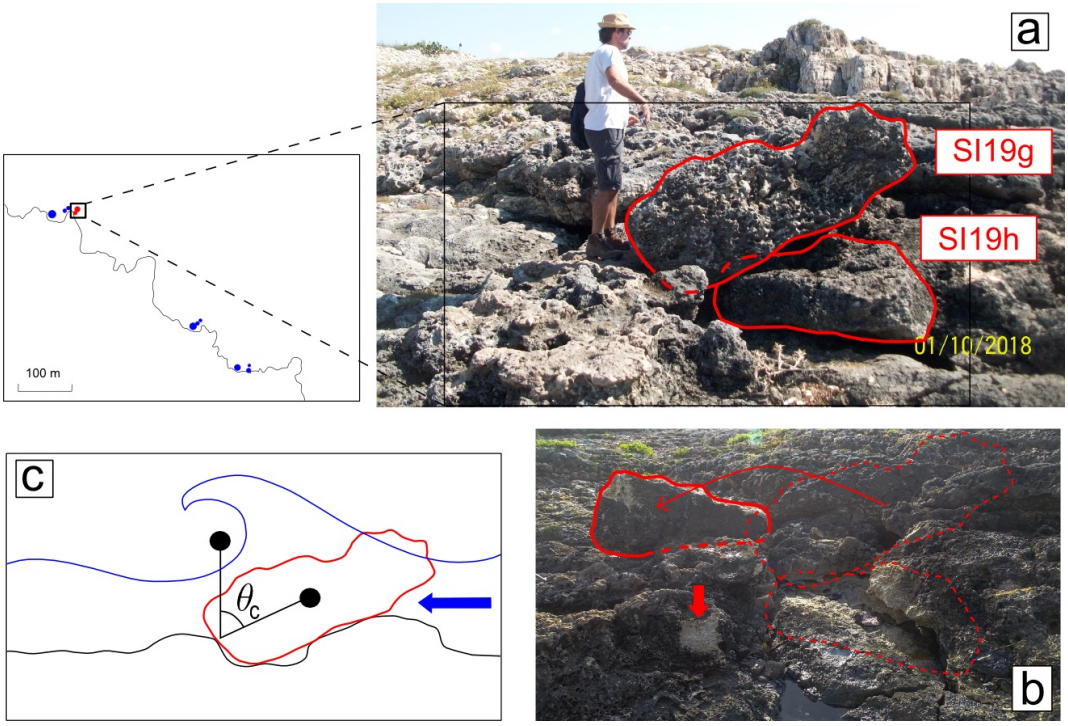

Figure A8. Comparison between pre- and post- storm event state; (a) pre-storm locations of boulders g and h; (b) post-storm overturned positions of boulder g (note the marks indicated by the arrow, probably the sign of the impact of a boulder on the bedrock); (c) angular threshold θ_c.

References

1. Hansom, J.D.; Switzer, A.D.; Pile, J. Extreme waves: causes, characteristics, and impact on coastal environments and society. In *Coastal and Marine Hazards, Risks, and Disasters*; Ellis, J.T; Sherman, D.J. Eds.; Elsevier: Netherlands, 2015, pp. 307-334.
2. You, Z.J. Tropical Cyclone-Induced Hazards Caused by Storm Surges and Large Waves on the Coast of China. *Geosciences* **2019**, *9*, 131.
3. Naylor, L.A.; Stephenson, W.J.; Smith, H.C.M.; Way, O.; Mendelssohn, J.; Cowley, A. Geomorphological control on boulder transport and coastal erosion before, during and after an extreme extra-tropical cyclone. *Earth Surf. Proc. Land.* **2016**, *41*, 685-700.
4. Huang, S.Y.; Yen, J.Y.; Wu, B.L.; Shih, N.W. Field observations of sediment transport across the rocky coast of east Taiwan: Impacts of extreme waves on the coastal morphology by Typhoon Soudelor. *Mar. Geol.* **2020**, *421*, 106088.
5. Süssmilch, C.A. Note on some recent marine erosion at Bondi. *Royal Soc. New South Wales J. Proc.* **1912**, *46*, 71–82.
6. Cox, R.; Zentner, D.B.; Kirchner, B.J.; Cook, M.S. Boulder ridges at the Aran Islands (Ireland): recent movements caused by storm waves, not tsunamis. *J. Geol.* **2012**, *120*, 249–272.
7. Mastronuzzi, G.; Sansò, P. Large boulder accumulation by extreme waves along the Adriatic coast of southern Apulia (Italy). *Quat. Int.* **2004**, *120*, 173–184.
8. Piscitelli, A.; Milella, M.; Hippolyte, J.C.; Shah-Hosseini, M.; Morhange, C.; Mastronuzzi, G. Numerical approach to the study of coastal boulders: The case of Martigues, Marseille, France. *Quat. Int.* **2017**, *439*, 52–64.
9. Scicchitano, G.; Scardino, G.; Tarascio, S.; Monaco, C.; Barracane, G.; Locuratolo, G.; Milella, M.; Piscitelli, A.; Mazza, G.; Mastronuzzi, G. The First Video Witness of Coastal Boulder Displacements Recorded during the Impact of Medicane "Zorbas" on Southeastern Sicily. *Water* **2020**, *12*, 1497.
10. Noormets, R.; Crook, K.A.W.; Felton, E.A. Sedimentology of rocky shorelines: 3. Hydrodynamics of megaclast emplacement and transport on a shore platform, Oahu, Hawaii. *Sediment. Geol.* **2004**, *10*, 41-65.
11. Goto, K.; Miyagi, K.; Kawana, T.; Takahashi, J.; Imamura, F. Emplacement and movement of boulders by known storm waves — Field evidence from the Okinawa Islands, Japan. *Mar. Geol.* **2011**, *283*, 66-78.
12. Maheras, P.; Flocas, H. A.; Patrikas, I.; Anagnostopoulou, Chr.. A 40 year objective climatology of surface cyclones in the Mediterranean region: spatial and temporal distribution. *Int. J. Climatol.* **2001**, *21*, 109-130.
13. Pirazzoli. P. A.; Tomasin, A.. Recent near-surface wind changes in the central Mediterranean and Adriatic areas. *Int. J. Climatol.* **2003**, *23*, 963-973.
14. Moscatello, A.; Miglietta, M.M.; Rotunno, R. Numerical Analysis of a Mediterranean "Hurricane" over Southeastern Italy. *Mon. Weather Rev.* **2008**, *136*, 4373-4397.
15. Fita, L.; Romero, R.; Luque, A.; Emanuel, K.; Ramis, C. Analysis of the environments of seven Mediterranean tropical-like storms using an axisymmetric, nonhydrostatic, cloud resolving model. *Nat. Hazards Earth Syst. Sci.* **2007**, *7*, 41-56.
16. Amores, A.; Marcos, M.; Carrió, D.S;.Gómez-Pujol, L. Coastal impacts of Storm Gloria (January 2020) over the north-western Mediterranean. *Nat. Hazards Earth Sys. Sci.* **2020**, *7*, 1955-1968.
17. Cavaleri, L.; Bajo, M.; Barbariol, F.; Bastianini, M.;Benetazzo, A.; Bertotti, L.; Chiggiato, J.; Davolio S.; Ferrarin, C.; Magnusson, L.; Papa, A.; Pezzutto, P.; Pomaro, P.; Umgiesser, G.. The October 29, 2018 storm in Northern Italy – An exceptional event and its modeling. *Prog. Oceanogr.* **2019**, *178*, 102178.
18. Ferrarin, C.; Valentini, A.; Vodopivec, M.; Klaric, D.; Massaro, G.; Bajo, M.; De Pascalis, F.; Fadini, A.; Ghezzo, M.; Menegon, S.; Bressan, L.; Unguendoli, S.; Fettich, A.; Jerman, J.; Ličer, M.; Fustar, L.; Papa, A.; Carraro, E. Integrated sea storm management strategy: the 29 October 2018 event in the Adriatic Sea. *Nat. Hazards Earth Sys. Sci.* **2020**, *20*, 73-93.
19. Androulidakis, Y.S.; Kombiadou, K.D.; Makris, C.V.; Baltikas, V.N.; Krestenitis, Y.N. Storm surges in the Mediterranean Sea Variability and trends under future climatic conditions. *Dynam. Atmos. Ocean.* **2015**, *71*, 56.
20. Romera, R.; Gaertner, M.A.; Sánchez, E.; Domínguez, M.; González-Alemán, J.J.; Miglietta, M.M. Climate change projections of medicanes with a large multi-model ensemble of regional climate models. *Global Planet. Change* **2017**, *151*, 134 - 143.

21. González-Alemán, J.J.; Pascale, S.; Gutierrez-Fernandez, J.; Murakami, H.; Gaertner, M.; Vecchi, G.A.. Potential Increase in Hazard From Mediterranean Hurricane Activity With Global Warming. *Geophys. Res. Lett.* **2019**, *46*, 1754-1764.
22. Delle Rose, M.; Fidelibus, C.; Miglietta, M. M.. Cambiamento climatico e protezione delle coste. *Ithaca, viaggio nella scienza* **2020**, *15*, 47-55 (in Italian).
23. Ciricugno, L.; Delle Rose, M.; Fidelibus, C.; Orlanducci, L.; Mangia, M.. Sullo spostamento di massi costieri causato da onde "estreme" (costa ionica salentina). *Geologi e Territorio* **2019**, *16*, 15–23 (in Italian).
24. Doglioni, C.; Tropeano, M.; Mongelli, F.; Pieri, P. Middle-Late Pleistocene uplift of Puglia: An "anomaly" in the Apenninic foreland. *Mem. Soc. Geol. It.* **1996**, *51*, 101–117.
25. Mastronuzzi, G.; Sansò, P. Boulders transport by catastrophic waves along the Ionian coast of Apulia (southern Italy). *Mar. Geol.* **2000**, *170*, 93–103.
26. Delle Rose, M.; Fidelibus, C.; Orlanducci, L. Ipotesi sullo spostamento di massi costieri per effetto di onde di bore. *Geologia dell'Ambiente* **2020**, *28(3)*, 21-27 (in Italian).
27. Dai Pra, G. The Late Pleistocene marine deposits of Torre Castiglione (Southern Italy). *Geogr. Fis. Din. Quat.* **1992**, *5*, 115–119.
28. Delle Rose, M.; Federico, A. Karstic phenomena and environmental hazard in the Salento coastal plains (Southern Italy). In *Proceedings of 9th International Associate Engineering Geology Congress*. Durban, South Africa, 2002; pp. 1297–1305.
29. Morucci, S.; Picone M.; Nardone, G.; Arena, G. Tides and waves in the central Mediterranean Sea. *J. Oper. Oceanogr.* **2016**, *9*, s10-s17.
30. Dentale, F.; Furcolo, P.; Pugliese Carratelli, E.; Reale, F.; Contestabile, P.; Tomasicchio G.R. Extreme wave analysis by integrating model and wave buoy data. *Water* **2018**, *10*, 373.
31. Trini Castelli, S.; Bisignano, A.; Donateo, A.; Landi, T.C.; Martano, P.; Malguzzi, P. Evaluation of the turbulence parametrization in the MOLOCH meteorological models. *Q. J. R. Meteorol. Soc.* **2019**, *146*, 124–140.
32. GLOBO-BOLAM-MOLOCH Forecast. Available online: http://www.isac.cnr.it/dinamica/projects/forecasts/index (accessed on 15 November 2019).
33. Istituto Superiore Protezione e Ricerca Ambientale: Dinamica e anomalia dell'evento del 12 novembre 2019 (in Italian). Available online: http://www.ismar.cnr.it/file/news-e-eventi/Dati (accessed on 04 August 2020).
34. Greece Extreme Weather: Medicane features, stormy winds up to 10 Beaufort. Available online: https://www.keeptalkinggreece.com/2019/11/11/greece-extreme-weather-medicane-10beaufort-ionian/ (accessed on 29 July 2020).
35. Sistema Informativo Meteo Oceanografico delle coste Pugliesi (SIMOP). Available online: http://93.51.158.171/web/simop/misure (accessed on 16 May 2020).
36. OGIMET Weather Information Service. Available online: https://www.ogimet.com/home.phtml.en (accessed on 11 December 2019).
37. Blott, S.G.; Pye, K. Particle shape: a review and new methods of characterization and classification. *Sedimentology* **2008**, *55*, 31-63.
38. Hsu, S.A., Ed. *Coastal Meteorology*; Academic Press, US; 260 pp., 1988.
39. Burroughs, L. Wave forecasting by manual methods. In *Guide to wave analysis and forecasting*; World Meteorological Organization, Eds. Secretariat of World Meteorological Organization, Switzerland, pp. 43-56, 1998.
40. Barua, D.K. Wave Hindcasting. In *Encyclopedia of Coastal Science*; Finkl, C.W.; Makowski, C., Eds. Springer International Publishing, Germany, pp. 1859-1864, 2019.
41. Owens, E.H. Sea Conditions. In *Beaches and Coastal Geology*; Springer, US, 722, 1984.
42. Knight, J.; Burningham, H. Boulder dynamics on an Atlantic-facing rock coastline, northwest Ireland. *Mar. Geol.* **2011**, *283*, 56-65.
43. Nandasena, N.A.K.; Paris, R.; Tanaka, N.. Reassessment of hydrodynamic equations: Minimum flow velocity to initiate boulder transport by high energy events (storms, tsunamis). *Mar. Geol.* **2011**, *281*, 70-84.
44. Imamura, F.; Goto, K.; Ohkubo, S.A numerical model for the transport of a boulder by tsunami *J. Geophys. Res. Oceans* **2008**, *113*, C01008.

45. Engel, M.; May, S.M. Bonaire's boulder fields revisited: evidence for Holocene tsunami impact on the Leeward Antilles. *Quat. Sci. Rev.* **2012**, *54*, 126-141.
46. Biolchi, S.; Furlani, S.; Devoto, S.; Scicchitano, G.; Korbar, T.; Vilibic, I.; Sepic, J. The origin and dynamics of coastal boulders in a semi-enclosed shallow basin: A northern Adriatic case study. *Mar. Geol.* **2019**, *411*, 62-77.
47. Pignatelli, C.; Sansò, P.; Mastronuzzi, G. Evaluation of tsunami flooding using geomorphologic evidence. *Mar. Geol.* **2009**, *260*, 6-18.
48. Vann Jones, E.C.; Rosser, N.J.; Brain, M.J. Alongshore variability in wave energy transfer to coastal cliff. *Geomorphology* **2018**, *322*, 1-14.
49. Cox, R.; Ardhuin, F.; Dias, F.; Autret, R.; Beisiegel, N.; Earlie, C.S.; Herterich, J.G.; Kennedy, A.; Paris, R.; Raby, A.; Schmitt, P.; Weiss, R. Systematic Review Shows That Work Done by Storm Waves Can Be Misinterpreted as Tsunami-Related Because Commonly Used Hydrodynamic Equations Are Flawed. *Front. Mar. Sci.* **2020**, *7*, 4.
50. Weiss, R.; Diplas, P. Untangling boulder dislodgement in storms and tsunamis: Is it possible with simple theories? *Geochem. Geophys. Geosyst.* **2015**, *16*, 890-898.
51. Herterich, J.G.; Cox, R.; Dias. F. How does wave impact generate large boulders? Modelling hydraulic fracture of cliffs and shore platforms. *Mar. Geol.* **2018**, *399*, 34-46.
52. Hibberd, S.; Peregrine, D.H. Surf and run-up on a beach: a uniform bore. *J. Fluid Mech.* **1979**, *95*, 323–345.
53. Cox, J.C.; Machemehl, J. Overload bore propagation due to an overtopping wave. *J. Waterw. Port Coast. Ocean Eng.* **1986**, *112*, 161–163.
54. Whittaker, C.N.; Fitzgerald, C.J.; Raby, A.C.; Taylor, P.H.; Borthwick, A.G.L. Extreme coastal responses using focused weve groups: Overtopping and horizontal forces exerted on an inclined seawall. *Coast. Eng.* **2018**, *140*, 292-305.
55. Roeber, V.; Bricker, J.D. Destructive tsunami-like wave generated by surf beat over a coral reef during Typhoon Haiyan. *Nat. Commun.* **2015**, *6*, 7854.
56. Cox, R.; Jahn, K.L.; Watkins. O.G.; Cox, P.. Extraordinary boulder transport by storm waves (west of Ireland, winter 2013-2014), and criteria for analysing coastal boulder deposits. *Earth Sci. Rev.* **2018**, *177*, 623-636.
57. Zainali, A.; Weiss, R. Boulder dislodgement and transport by solitary waves: Insights from three-dimensional numerical simulations. *Geophys. Res. Lett.* **2015**, *42*, 4490-4497.
58. Carbone, F.; Dutykh, D.; Dudley, J.M.; Dias, F. Extreme wave runup on a vertical cliff. *Geophys. Res. Lett.* **2013**, *40*, 3138-3143.
59. Paris, R.; Naylor, L.A.; Stephenson, W.J.S. Boulders as a signature of storms on rock coasts. *Mar. Geol.* **2011**, *283*, 1–11.
60. Sunamura T. Rocky coast processes: with special reference to the recession of soft rock cliffs. In *P. Jpn Acad. B-Phys., 91*; Japan Academy, Japan, pp. 481–500, 2015.
61. Wolters, G.; Muller, G. The propagation of wave impact induced pressures into cracks and fissure. *Geol. Soc. Lond. Eng. Geol. Spec. Publ.* **2004**, *20*, 121–130.

Sample Availability: Photograph survey documentation is available from M.D.R.